 CMES, vol.2, no.4, pp.509-522, 2001

An Improved Contact Algorithm for the Material Point Method and Application to Stress Propagation in Granular Material

S.G. Bardenhagen[1] and J.E. Guilkey[2] and K.M. Roessig[3] and J.U. Brackbill[4] and W.M. Witzel[5] and J.C. Foster[6]

Abstract: Contact between deformable bodies is a difficult problem in the analysis of engineering systems. A new approach to contact has been implemented using the Material Point Method for solid mechanics, Bardenhagen, Brackbill, and Sulsky (2000a). Here two improvements to the algorithm are described. The first is to include the normal traction in the contact logic to more appropriately determine the free separation criterion. The second is to provide numerical stability by scaling the contact impulse when computational grid information is suspect, a condition which can be expected to occur occasionally as material bodies move through the computational grid. The modifications described preserve important properties of the original algorithm, namely conservation of momentum, and the use of global quantities which obviate the need for neighbor searches and result in the computational cost scaling linearly with the number of contacting bodies. The algorithm is demonstrated on several examples. Deformable body solutions compare favorably with several problems which, for rigid bodies, have analytical solutions. A much more demanding simulation of stress propagation through idealized granular material, for which high fidelity data has been obtained, is examined in detail. Excellent qualitative agreement is found for a variety of contact conditions. Important material parameters needed for more quantitative comparisons are identified.

[1] Dept. of Mechanical Engineering, University of Utah, Salt Lake City, UT 84112, USA. Presently on leave from Group ESA–EA, MS P946, Los Alamos National Laboratory, Los Alamos, NM

[2] Dept. of Mechanical Engineering, University of Utah, Salt Lake City, UT 84112, USA.

[3] Air Force Research Laboratory, Munitions Directorate, Eglin AFB, FL 32542, USA.

[4] Theoretical Division, Los Alamos National Laboratory, Los Alamos, NM 87545, USA

[5] Dept. of Computer Science, University of Utah, Salt Lake City, UT 84112, USA.

[6] Air Force Research Laboratory, Munitions Directorate, Eglin AFB, FL 32542, USA.

keyword: Contact Algorithm, Material Point Method, Wave Propagation, Granular Material.

1 Introduction

With continued growth of computational power, numerical analysis techniques are being extensively applied to engineering systems, rather than just individual components. The promise of reducing costs during design and testing is enticing, but remains difficult to realize in practice. Extensive effort has been expended to develop accurate material models and solution techniques for complex boundary value problems involving individual components and pinned or welded structures. In the more general arena of engineering systems, however, components often contact and slide against one another. Contact mechanics is remarkably difficult, both due to potentially applicable physics, and mathematical complexities associated with solution constraint inequalities, as discussed in the review article by Barber and Ciavarella (2000).

When engineering systems function within designed operating conditions severe contact is usually avoided, but it is of paramount interest in evaluating system response during severe loading and/or failure. Classic examples include car crashes, aircraft engine fan blade containment, and earth penetrators. Contact and impact have received substantial attention over the past several decades, as witnessed by a review of the subject by Zhong and Mackerie (1994), which lists nearly 500 papers. The majority of these papers describe numerical modeling approaches and/or applications using the finite element method. The problem is a very difficult one, as contact must be sensed, surface normals constructed, and interaction forces imposed to prevent interpenetration without making the system of equations to be solved ill–conditioned.

For large scale engineering simulations contact is frequently the aspect which must be tweaked by the ana-

lyst, using various loosely physical parameters, just to get the simulation to run. In addition the algorithms are traditionally expensive. Effective numerical simulation of engineering systems is in need of further development of accurate, efficient contact algorithms. Here we describe an alternate approach using a particle–in–cell (PIC) numerical technique for solid mechanics, the Material Point Method, Sulsky, Chen, and Schreyer (1994); Sulsky, Zhou, and Schreyer (1995); Sulsky and Schreyer (1996).

The Material Point Method (MPM) is one of the latest developments in several decades of particle–in–cell methods, originally used to model highly distorted fluid flow, Harlow (1963). Subsequent developments advanced the understanding of the algorithm and brought modifications to reduce numerical diffusion, Brackbill, Kothe, and Ruppel (1988); Burgess, Sulsky, and Brackbill (1992). Fundamental aspects of PIC methods include the interpolation of information between grid and particles, and precisely which solution variables will be ascribed to the grid, and which to the particles. Several variants have been tried, with a general trend toward keeping more properties on particles. Most recently, the method has been applied to solid mechanics, where the ability of the particles, or "material points", to advect naturally Lagrangian state variables, has been exploited in MPM.

Recently a new approach to material contact has been developed and used with MPM, Bardenhagen, Brackbill, and Sulsky (2000a). This approach takes advantage of the Arbitrary Lagrangian/Eulerian (ALE) formulation of MPM which tracks Lagrangian particle motion through an Eulerian grid. Coulomb friction contact conditions are applied via the grid. The approach has been demonstrated using two–dimensional calculations of collisions and the shearing of granular material, Bardenhagen, Brackbill, and Sulsky (2000a,b,c). Here an essential modification to the physics of the algorithm is described, as well as a modification for numerical stability. The algorithm is demonstrated on simple problems in three–dimensions with analytical solutions. Finally it is applied to stress wave propagation in simple granular materials.

2 Approach

MPM is briefly reviewed here for completeness. Lagrangian bodies are discretized into material points, which carry all information required to specify the current state and advance the solution. This information includes constitutive parameters (such as moduli and internal variables), stress, strain, velocity and temperature. The MPM algorithm also uses a computational grid. The governing equations are solved on the grid, providing a computational savings and as well as a regular, structured grid on which to apply solution techniques. See Fig. 1 for an example of the discrete representation of a disk, where material points and mesh are shown. The coupling between the material points and the mesh is a key ingredient in the solution algorithm. Quantities are interpolated between the mesh and the material points such that total mass and momentum are conserved. Advantages of the MPM algorithm include the absence of mesh tangling problems, error–free advection of material properties (internal variables in particular) via the motion of the material points, and an efficient setting for the implementation of material contact.

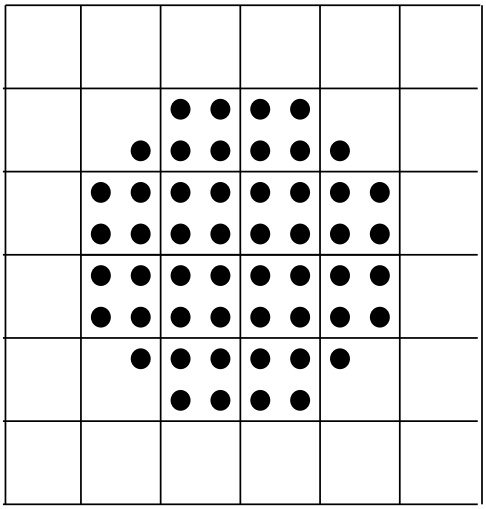

Figure 1 : Simple example of a material point discretization of a disk.

Bodies deform according to continuum mechanics constitutive models and conservation laws. If $\rho(\mathbf{x},t)$ is the mass density at point $\mathbf{x}$ at time t, and $\mathbf{v}(\mathbf{x},t)$ is the velocity field, then conservation of mass is

$$\frac{d\rho}{dt} = -\rho\nabla\cdot\mathbf{v}, \tag{1}$$

in which the time derivative is the material derivative

$$\frac{d}{dt} = \frac{\partial}{\partial t} + \mathbf{v}\cdot\nabla. \tag{2}$$

Conservation of mass is satisfied implicitly in MPM. Material points are assigned fixed masses during the initial discretization, and grid masses are determined using an interpolation scheme which conserves mass. Conservation of momentum is

$$\rho \frac{d\mathbf{v}}{dt} = \nabla \cdot \boldsymbol{\sigma}, \tag{3}$$

where $\boldsymbol{\sigma}$ is the Cauchy stress tensor. Different materials are modeled via constitutive equations that generate stress based on both the history and current mechanical state. Versions of hyperelasticity, hypoelasticity, plasticity and viscoelasticity have been implemented, Sulsky, Chen, and Schreyer (1994); Sulsky, Zhou, and Schreyer (1995); Sulsky and Schreyer (1996); Bardenhagen, Brackbill, and Sulsky (2000b); Bardenhagen and Brackbill (1998); Bardenhagen, Harstad, Maudlin, Gray, and Foster (1998). Conservation of momentum is solved on the grid and changes are interpolated to the material points such that the change in momentum is the same on the grid and on the material points. Interpolating only changes in momentum reduces numerical diffusion, Brackbill, Kothe, and Ruppel (1988). Energy conservation errors are proportional to the square of the time step, Brackbill and Ruppel (1986); Bardenhagen (2001). Details of the explicit computational algorithm may be found in the references, Sulsky, Chen, and Schreyer (1994); Sulsky, Zhou, and Schreyer (1995); Sulsky and Schreyer (1996).

Interactions between bodies are modeled using a contact algorithm which forbids inter–penetration, but allows separation, sliding with friction, and rolling. A previous version of the algorithm, in which the logic was based completely on kinematics, was detailed in, Bardenhagen, Brackbill, and Sulsky (2000a). Here an essential modification to the original formulation is described. In addition, a useful means of screening out the application of large contact forces, numerical errors due to unfortunate registration of material point information on the computational grid, is described. These changes provide for a more accurate and robust algorithm.

2.1 Contact Algorithm Logic Refinements

Recall that contact is modeled on the computational grid in MPM. The mass and momentum from material points are interpolated to the computational grid for each body. Individual body velocities are computed by taking the ratio of momentum, $\mathbf{p}^\alpha$, to mass, m^α, at the grid nodes, i.e.,

$$\mathbf{v}^\alpha = \frac{\mathbf{p}^\alpha}{m^\alpha} \qquad \alpha = 1, 2, \ldots, N, \tag{4}$$

where α indexes the bodies and N is the number of bodies in a computation. The average velocity of *all* material points in the vicinity of a grid node is termed the center of mass velocity and denoted $\mathbf{v}^{cm}$

$$\mathbf{v}^{cm} = \sum_{\alpha=1}^{N} \frac{\mathbf{p}^\alpha}{M}, \tag{5}$$

where

$$M = \sum_{\alpha=1}^{N} m^\alpha, \tag{6}$$

is the total mass contribution from all bodies in the vicinity of a grid node. The center of mass velocity and the total mass are the global quantities which enable the determination of contact grid nodes and precisely what the contact constraints should be. Nodes in the vicinity of more than one body are detected by looking at the difference between individual body and center of mass velocities. Interface computational grid nodes are defined as those for which

$$\mathbf{v}^{cm} - \mathbf{v}^\alpha \neq \mathbf{0}. \tag{7}$$

Resolution of the interface is commensurate with the computational grid cell size.

Once a contact grid node has been identified, further analysis is required to determine what contact condition should be applied (sticking or slipping contact, or free separation). Spatial differentiation of the individual body masses on the grid, m^α, provides a computation of the body surface normals $\mathbf{n}^\alpha$. Using the surface normals, approach and departure can be distinguished. A body is approaching its neighbor(s) when

$$(\mathbf{v}^\alpha - \mathbf{v}^{cm}) \cdot \mathbf{n}^\alpha > 0. \tag{8}$$

For the algorithm described previously, Bardenhagen, Brackbill, and Sulsky (2000a), sticking or slipping contact constraints are applied if approach is detected, otherwise free separation is allowed.

It is the use of normal traction information which distinguishes this algorithm from that described previously, Bardenhagen, Brackbill, and Sulsky (2000a). The normal surface traction, t_n^α, is computed at a contact grid

node by interpolating individual material point contributions using the surface normals (and the relation $t_n^\alpha = \mathbf{n}^\alpha \cdot \boldsymbol{\sigma}^\alpha \cdot \mathbf{n}^\alpha$). In the special case where contacting bodies are stress free (e.g. when first coming into contact) it is sufficient to determine which contact condition to apply based strictly on whether or not bodies are approaching. When the normal tractions are non–zero, it is important to distinguish between compressive and tensile interface tractions. For the sign convention used here compressive stress is negative and the normal traction is compressive when

$$t_n^\alpha < 0. \tag{9}$$

The essential modification to the contact algorithm logic is to *apply frictional contact when the normal traction is compressive*, allowing free separation otherwise. Frictional contact is applied via constraints on the body velocities $\mathbf{v}^\alpha$. Free separation requires that no constraints be prescribed. Note that the efficiency of the algorithm is not compromised by the additional logic involving the normal traction. Calculation of contact conditions in the center of mass frame eliminates a separate contact detection step, achieves a solution with one sweep through the computational grid, and yields a linear scaling of the computational cost with the number of bodies, Bardenhagen, Brackbill, and Sulsky (2000a). It is also worth noting that the complexity of the contact algorithm does not increase if the shape of the bodies are varied, so complex initial geometries and large deformations can easily be modeled.

Using the simple example of a deformable body colliding with a rigid boundary, it may be seen that simply monitoring approach and departure is insufficient to model contact correctly. As the body approaches the boundary the compressive traction builds, and by either kinematic or normal traction criteria, frictional contact conditions would be applied. Application of the frictional contact constraints is equivalent to an instantaneous inelastic collision, serving to exchange kinetic and strain energies. The essential difference occurs during rebound. If free separation is prescribed as soon as departure begins, the equivalent scenario is instantaneous removal of the boundary. Rather, the normal traction must be monitored and frictional contact with the boundary applied while it remains compressive. Free separation is allowed once the normal traction is non–negative. This modification provides for the extraction of strain energy on departure, much like it provides for strain energy buildup during approach. Without this logic modification, frictionless collisions were found to slightly increase system energy. Although the logic is not described in detail there, the modified algorithm was found to be slightly dissipative Bardenhagen, Brackbill, and Sulsky (2000c).

When applied to contact between deformable bodies the situation is very similar to that described for a rigid boundary when both have the same material response. Enforcement of no interpenetration during contact is applied by constraining the body velocity component normal to the surface to be equal to the center of mass velocity in that direction. This is equivalent to a uniform stretch assumption in the surface normal direction. Because different materials respond to the same stretch with different stresses, the normal tractions which develop during contact will likely be different for different bodies. It is even possible that uniform un–straining will result in bodies of different materials experiencing free separation at different times during departure, particularly when material response allows for permanent set (e.g. plasticity). Although traction equilibrium is not maintained at contact nodes, interfaces are unloaded to their stress free state. This source of error could be eliminated in an implicit formulation of MPM where the appropriate partitioning of strain increments between bodies for traction equilibrium would be determined.

2.2 Numerical Considerations

A practical consideration arises in the application of an MPM algorithm which uses grid node variables. Namely, interpolated values can be very small when a grid node first begins to represent material point data. This can occur when a body's material points first cross into cells which previously contained no material points from that body. Because this happens at the edges of bodies, it is an especially important consideration in the application of contact conditions.

Frictional contact conditions are applied by assigning new grid velocities, $\tilde{\mathbf{v}}^\alpha$, after contact

$$\tilde{\mathbf{v}}^\alpha = \mathbf{v}^\alpha - \Delta v_n^\alpha (\mathbf{n}^\alpha + \mu' \mathbf{t}^\alpha), \qquad \mu' = \min\left(\mu, \frac{\Delta v_t^\alpha}{\Delta v_n^\alpha}\right) \tag{10}$$

where μ is the interfacial coefficient of friction, $\mathbf{t}^\alpha$ is the unit tangent in the direction of sliding ($\mathbf{t} = \boldsymbol{\omega} \times \mathbf{n}$ in Bardenhagen, Brackbill, and Sulsky (2000a)), and

$$\Delta \mathbf{v}^\alpha = \mathbf{v}^\alpha - \mathbf{v}^{cm}, \tag{11}$$

$$\Delta v_n^\alpha = \Delta \mathbf{v}^\alpha \cdot \mathbf{n}^\alpha, \tag{12}$$

$$\Delta v_t^\alpha = \Delta \mathbf{v}^\alpha \cdot \mathbf{t}^\alpha, \tag{13}$$

as described in detail in Bardenhagen, Brackbill, and Sulsky (2000a).

Resolution of the topology of contacting surfaces on the computational grid requires no more than two bodies be represented at a contact grid node. The remaining contact node analyses are specialized for $N = 2$. It should be noted that not all of the properties derived below hold for $N > 2$. The definition of the center of mass velocity, $\mathbf{v}^{cm}$, Eqn. 5, gives the useful identity

$$\sum_{\alpha=1}^{2} m^\alpha \Delta \mathbf{v}^\alpha = \mathbf{0}, \tag{14}$$

from which it can be seen that $\Delta v_t^1/\Delta v_n^1 = \Delta v_t^2/\Delta v_n^2$, i.e. either both bodies stick or both bodies slip.

When the effective coefficient of friction, μ', in Eqn. 10 is not limited by the interfacial friction coefficient, μ, the surfaces stick. It is easy to show that for this case the contact algorithm conserves momentum exactly. The total momentum change imposed by applying sticking contact is

$$\sum_{\alpha=1}^{2} m^\alpha (\tilde{\mathbf{v}}^\alpha - \mathbf{v}^\alpha) = -\sum_{\alpha=1}^{2} m^\alpha \Delta \mathbf{v}^\alpha = \mathbf{0}. \tag{15}$$

where Eqn 14 has been used. For slipping contact, the sum of momenta on the grid gives

$$\begin{aligned}\sum_{\alpha=1}^{2} m^\alpha (\tilde{\mathbf{v}}^\alpha - \mathbf{v}^\alpha) = &-\sum_{\alpha=1}^{2} m^\alpha \Delta \mathbf{v}^\alpha \cdot \mathbf{n}^\alpha \mathbf{n}^\alpha \\ &- \mu \sum_{\alpha=1}^{2} m^\alpha \Delta \mathbf{v}^\alpha \cdot \mathbf{n}^\alpha \mathbf{t}^\alpha.\end{aligned} \tag{16}$$

While in general slipping contact does not conserve momentum, the errors are associated with non–collinearity in the calculation of body normals and tangents, i.e. poor resolution of interface curvature. For $\mathbf{n}^2 = -\mathbf{n}^1$ and $\mathbf{t}^2 = -\mathbf{t}^1$, momentum is conserved exactly (from Eqn. 14).

A common scenario as two bodies approach and depart is for the grid mass of one body to approach zero while the other remains finite. If, through unfortunate registration of material point mass on the computational grid, a body's grid mass is very small, the resulting change in velocity prescribed by the contact algorithm may be very large. This result can be seen from Eqn. 15, for example. Working with momenta, rather than velocities, is an elegant solution for updating material point positions and velocities in this case, Sulsky, Zhou, and Schreyer (1995). However, calculations of material point incremental strains require velocities on the grid in order to differentiate it there, and remain problematic. In practice these unfortunate registration events are marked by abrupt changes in the kinematics of the contacting bodies, the occurance of which is time step size dependent.

An effective stability criterion has been developed which is loosely analogous to the Courant explicit time stepping criterion. The Courant condition demands that solution information not be allowed to propagate across more than one cell in a single time step. Similarly, for the contact algorithm the instantaneous change in velocity must not be large enough to collapse (or invert) a computational cell. Define the instantaneous strain rate imposed by the contact algorithm

$$\dot{\boldsymbol{\varepsilon}}_j^\alpha = \frac{\tilde{v}_j^\alpha - v_j^\alpha}{\Delta x_j} \tag{17}$$

where Δx_j is the grid spacing in each coordinate direction. Then the condition that the contact strain increment not collapse a neighboring cell in one time step is

$$\dot{\boldsymbol{\varepsilon}}_{max}^\alpha \Delta t < 1 \tag{18}$$

where $\dot{\boldsymbol{\varepsilon}}_{max}^\alpha = \max_j |\dot{\boldsymbol{\varepsilon}}_j^\alpha|$. Using Eqn. 14, the grid strain rates for each body may be related, e.g.

$$\dot{\boldsymbol{\varepsilon}}_j^2 = -\frac{m^1}{m^2}\dot{\boldsymbol{\varepsilon}}_j^1 = \frac{m^1}{M - m^1}\dot{\boldsymbol{\varepsilon}}_j^1. \tag{19}$$

These relations allow the most severe grid strain rate, for either material, to be calculated independently

$$\dot{\boldsymbol{\varepsilon}}_{max} = \max_j \left(\max\left(\frac{m^\alpha}{M - m^\alpha}, 1 \right) |\dot{\boldsymbol{\varepsilon}}_j^\alpha| \right). \tag{20}$$

Only global grid quantities and quantities specific to the body under consideration are needed in the calculation.

In practice, Eqn. 18 is modified to provide a safety factor,

$$\dot{\boldsymbol{\varepsilon}}_{max} \Delta t < \gamma \qquad 0 < \gamma \leq 1. \tag{21}$$

Implementation of the collapsed cell stability condition is achieved by scaling the velocity change imposed by the contact algorithm when necessary

$$\tilde{\mathbf{v}}_{scaled}^\alpha = \mathbf{v}^\alpha - \max\left(\frac{\gamma}{\dot{\boldsymbol{\varepsilon}}_{max} \Delta t}, 1 \right) \Delta v_n^\alpha (\mathbf{n}^\alpha + \mu' \mathbf{t}^\alpha). \tag{22}$$

The most severe constraint, for either body, can be determined using only quantities specific to the body under consideration, and global quantities, retaining the efficiency of the original formulation. In addition, the scaling preserves the momentum conservation properties of the algorithm, Eqn.s 15 and 16.

Note that large grid strain increments occur at grid nodes for which the value of the interpolating functions are small (resulting in a small grid mass there). Because the same weighting is used to interpolate strain increments from the grid back to the material points, material point strain increments will be *much* smaller. If grid velocities are unaltered by the contact algorithm, interpolation from material points to grid and back again scales out, and material point strains are well behaved regardless of the registration of material point information on the grid. It is only when the grid velocities are adjusted that particle strain calculations can be problematic, Sulsky, Zhou, and Schreyer (1995).

The approach described meets the cell collapse constraint, Eqn. 21, by systematically limiting the maximum grid strain rate. Consideration was also given to the obvious alternative, simply reducing the current time step size, and restarting the time step. This alternative was rejected because it is the initial registration of the particle data on the grid which is ultimately responsible for large grid strain rates. These rates are computational artifacts, traceable ultimately to the low order of the interpolation scheme used to develop grid data. A remedy of this sort would more appropriately be applied to the *previous* time step size. However, without a search to locate material points near grid boundaries, there is no way to guarantee avoiding the problem at all grid nodes simultaneously. The above described algorithm provides an efficient means of improving accuracy by screening out computational artifacts.

3 Applications

To demonstrate the accuracy of the contact algorithm, numerical solutions are first compared to analytical ones from rigid body dynamics. A more complex example is provided by simulating stress wave propagation in idealized granular material. For all cases, the contact algorithm scale factor γ was taken to be 0.5. Little sensitivity to the scale factor was seen in the range $.5 \leq \gamma \leq 1$. However, for $\gamma < 0.5$ bodies were observed to penetrate to varying degrees during contact. Based on this experience, a recommended range is $.5 \leq \gamma \leq 1$.

3.1 Sphere Rolling on an Inclined Plane

For a simple test of the algorithm, a sphere rolling down a flat inclined plane is simulated. The simulation is performed in 3–dimensions. A symmetry plane exists, and the simulation direction perpendicular to that plane serves only to distinguish the geometry (a sphere rather than a cylinder). See Fig. 2 for the problem setup. The x– and z–directions lie in the plane of symmetry with x in the direction of rolling and z perpendicular. The radius of the sphere, R, is 1.6 m, and the length of the plane on which it rolls is 20 m. The incline of the plane is described by the angle between the z–direction and that of gravity, θ. For all calculations the acceleration due to gravity is taken to be 10 m/s^2. The inclined plane problem has exact solutions for a rigid sphere on a rigid plane.

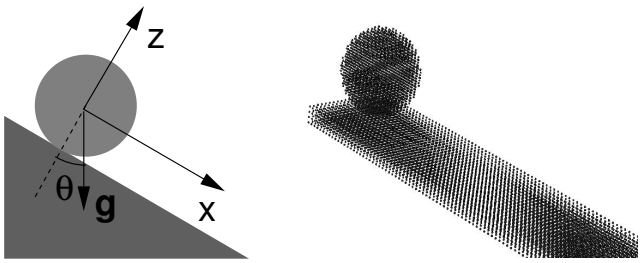

Figure 2 : Schematic of the inclined plane problem and $R/4$ cell size MPM discretization.

In the simulations the sphere and plane are deformable. The grid is uniform with equal spacing in all directions and eight material points per cell. The cell sides are of length $R/4$, providing 8 computational cells across the diameter of the sphere. This discretization is depicted in Fig. 2. The material properties are chosen to allow for large time steps using an explicit code, and consequently correspond to a rather soft material. Both sphere and plane are modeled as compressible Neo–Hookean hyperelastic bodies, Simo and Hughes (1998). The sphere has bulk modulus 6 MPa, shear modulus 3 MPa, and density 1000 kg/m^3, roughly approximating those of a natural rubber. The plane has elastic constants and density an order of magnitude larger, resulting in a much stiffer material with the same wave speeds. The longitudinal wave speed is 100 m/s and a typical calculation for this resolution requires 500 time steps.

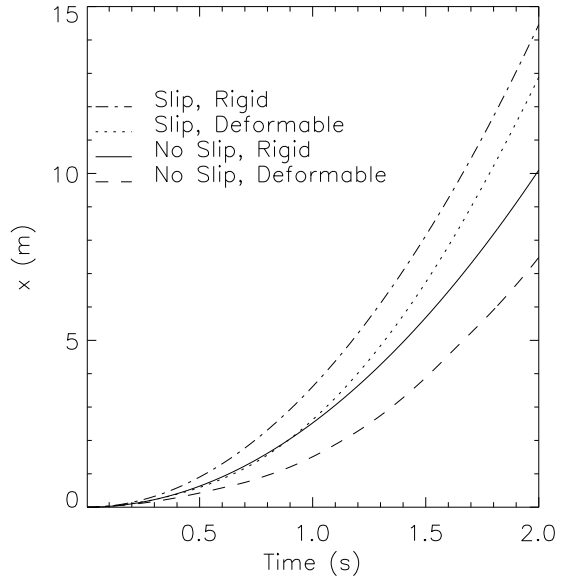

Figure 3 : Sphere center of mass x–position as a function of time for both the slip and no slip cases. The rigid sphere analytical solutions are shown for comparison.

Two cases are considered. For the first $\theta = \pi/4$ and the coefficient of friction is .495. This case is referred to as the "no slip" case because the rigid sphere solution describes rolling without slipping. For a rigid sphere the x–position of the center of mass is given by

$$x(t) = \frac{25\sqrt{2}}{14}t^2. \tag{23}$$

The center of mass position of the deformable sphere is depicted in Fig. 3, along with the analytical solution for comparison. For the second case $\theta = \pi/3$ and the coefficient of friction is .286. In this case the analytical solution describes rolling while sliding and is referred to as the "slip" case. For a rigid sphere the x–position of the center of mass is given by

$$x(t) = \frac{5}{2}(\sqrt{3} - \frac{2}{7})t^2, \tag{24}$$

The center of mass position for the deformable sphere, and the analytical solution for comparison, are also plotted in Fig. 3. For both cases the solutions are similar to their rigid sphere counterparts, with the deformable disks rolling and sliding more slowly. The slower motion of the deformable spheres is also seen in a plot of their center of mass velocities in the direction of rolling, Fig. 4. The abrupt changes in velocity, most evident in the no slip case, are due to the application of the contact algorithm.

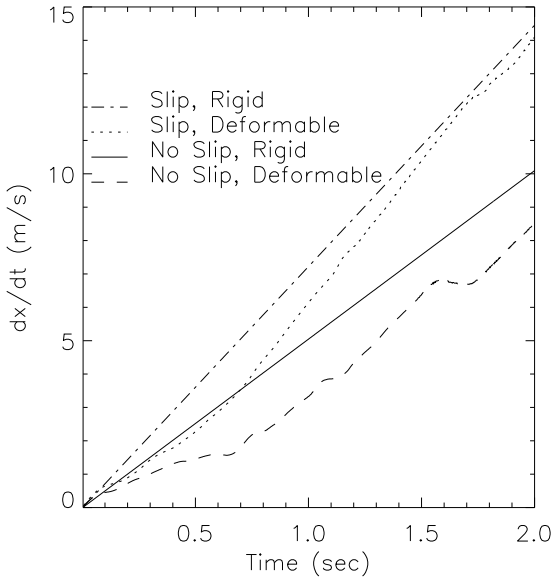

Figure 4 : Sphere center of mass x–velocity as a function of time for both the slip and no slip cases. The rigid sphere analytical solutions are shown for comparison.

Attention is now focused on the no slip case. To investigate the effect of spatial resolution this case was run with cell sizes $R/2$ and $R/8$, corresponding to 4 and 16 cells across the sphere diameter. The effect of spatial resolution on calculated position of the center of mass is depicted in Fig 5, where the analytical solution for a rigid sphere appears on the graph for reference. Simulations for the deformable case are labeled by cell size. The lowest resolution case, $R/2$, is instructive. In this case the resolution is too crude to resolve the geometry on a rectangular grid and the sphere fails to roll because of a flat spot (the resolution is the three–dimensional equivalent of that depicted in Fig. 1). For the finer resolutions, $R/4$ and $R/8$, the geometry is sufficiently resolved to permit rolling and the solution quickly converges toward the rigid sphere case. It appears that although the material properties correspond to a very soft material, it is resolution of the geometry that is most important in this simulation.

The effect of spatial resolution on the sphere center of mass velocity is shown in Fig. 6. For the lowest resolution there is an indication of vibration about the initial

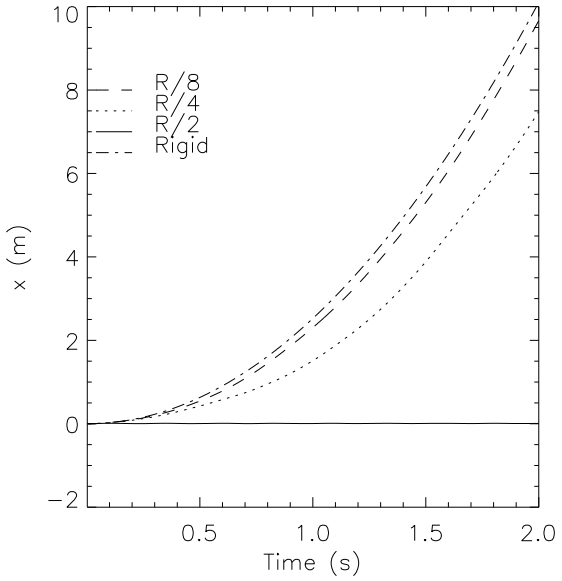

Figure 5 : No slip case sphere center of mass position as a function of time for various spatial resolutions. The rigid sphere analytical solution is shown for comparison.

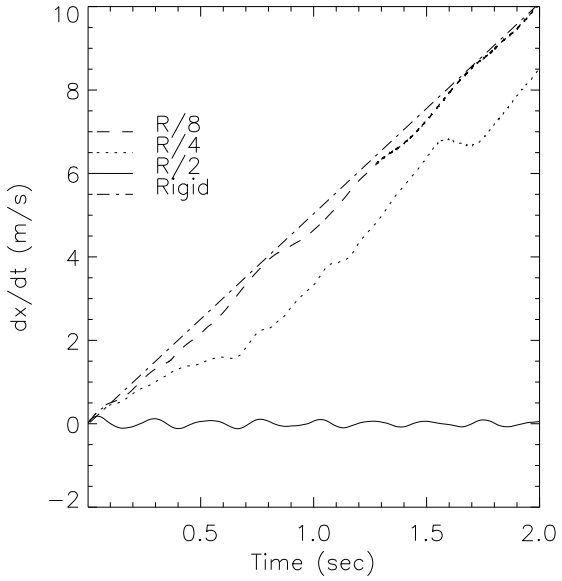

Figure 6 : No slip case sphere center of mass velocity as a function of time for various spatial resolutions. The rigid sphere analytical solution is shown for comparison.

configuration, but no rolling, as expected. For finer resolutions the sphere rolls, and the velocity converges toward the rigid sphere solution. The rigid sphere solution appears to provide an upper bound on the velocity for these simulations. This might be expected in part because potential energy is converted both to elastic (strain) energy and kinetic energy for the deformable sphere, while for the rigid case all potential energy is converted to kinetic energy. However, the sphere skips slightly, and while not in contact accelerates more quickly than while rolling in contact. If the simulation was carried out long enough, the sphere would eventually travel more quickly in the numerical simulation, due to skipping

3.2 Backspin Problem

A slightly more complex problem is the motion of an initially stationary, spinning sphere on a flat plane ($\theta = 0$) under gravity. Although spinning, the center of mass velocity is initially zero. This problem is termed the "backspin" problem. The same material properties and acceleration of gravity are used for this problem, but the sphere has unit radius and only the higher resolutions considered are used (cell sizes $R/4$ and $R/8$). The coefficient of friction is taken to be 0.5 and the initial angular velocity 5 rad/s.

Once again, for a rigid sphere there is an analytical solution. First the sphere slides and rolls while accelerating. When velocities at the contact point match it rolls without slipping at constant velocity. This solution for the center of mass position is given by

$$x(t) - x_0 = (5/2)t^2 \qquad t \leq 2/7, \tag{25}$$

$$x(t) - x_0 = (5/2)(2/7)^2 + (10/7)(t - 2/7) \qquad t > 2/7, \tag{26}$$

where $t = 2/7$ is the time at which slipping stops. Numerical simulation results for deformable spheres, as well as the rigid sphere solution, are shown in Figs. 7 and 8.

For both position and velocities, results converge toward the rigid sphere results, indicating the importance of resolving the geometry accurately. The deformability of the sphere plays a larger role at the higher angular velocities induced during this simulation. The combination of deformability and skipping produces the strong oscillations in center of mass velocity seen in Fig. 8. Analogous to stick–slip like behavior, the sphere catches briefly causing acceleration of the center of mass velocity, fol-

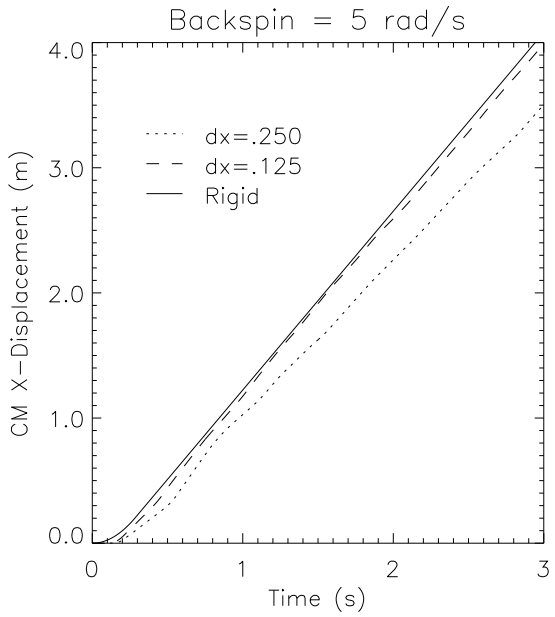

Figure 7 : Sphere center of mass position as a function of time for $R/4$ (labeled dx=.250) and $R/8$ (dx=.125) cell size MPM discretizations. The rigid sphere analytical solution is shown for comparison.

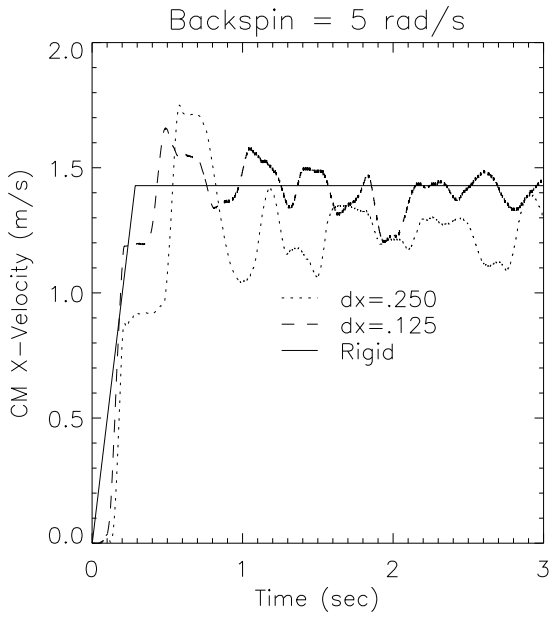

Figure 8 : Sphere center of mass velocity as a function of time for $R/4$ (labeled dx=.250) and $R/8$ (dx=.125) cell size MPM discretizations. The rigid sphere analytical solution is shown for comparison.

lowed by free spinning during which the velocity is essentially constant. The oscillations in velocity are due to deformability. When the sphere contacts with excessive forward spin, the center of mass velocity is increased and the sphere is compressed forward of the contact patch. As this strain energy is released during a skip (free flight), the sphere expands resulting in an increase in forward velocity at the following contact patch and an effective backspin, slowing the center of mass on contact.

3.3 Stress Waves In Granular Media

A significantly more demanding modeling problem is presented by calculating stress waves in granular media. This problem has been studied extensively by Shukla and co–workers, Rossmanith and Shukla (1982); Shukla and Damania (1987); Shukla (1991); Zhu, Shukla, and Sadd (1996), who used detonators to load collections of disks. Using photoelastic disks and high–speed photography, they were able to temporally and spatially resolve the stress state as the impulse traveled through various assemblages. More recently similar experiments have been undertaken, but using a Hopkinson bar to dynamically load the disks, Roessig (2001). In this case the loading results in a step change in velocity rather than an unsteady impulse of short duration. The latter is better characterized, and a much easier boundary condition to simulate.

Because frictional sliding is a defining characteristic of granular material, it is natural to test the contact algorithm by simulating granular material response. This was done previously for dynamic wave propagation, Bardenhagen and Brackbill (1998) and shearing deformations, Bardenhagen, Brackbill, and Sulsky (2000c,b) with very good qualitative "macroscopic" agreement. However, a direct comparison of experimental and numerical results for a specific microstructure was never made. Here results for well characterized assemblies of disks and loading conditions are simulated and compared to experimental measurements.

The experimental setup is facilitated by a mild steel loading frame which holds the disks. Dimensions adjust easily, allowing various geometries to be assembled. One–quarter inch grooves in the sides of the frame hold the disks in plane. Loading is applied via a split Hopkinson bar. The input pulse is recorded and analyzed to give a striker velocity, which for the experiments reported

here is 5.6 m/s. The disks are 2 inches in diameter, 1/4 inch thick, and made of Plexiglas. Experimental measurements are made using a high speed camera and the technique of photoelasticity. The camera is triggered by wave propagation in the Hopkinson bar prior to reaching the disks. The transfer of the stress wave to a loading pin of equal thickness as the disks ensures plane stress loading conditions. Unfortunately, this results in some uncertainty ($\pm 10\,\mu$s) in the arrival time of the stress wave at the first disks ("impact"). However, interframe times are much more precise, and provide the more exacting constraint on the comparisons. Photoelasticity generates dark fringes at contours of constant maximum shear stress. Because in the simulations the spatial variation of the stress state is known, it is straight–forward to do the corresponding calculation. Specifically, the stress tensor is diagonalized. For isotropic response the the out–of–plane direction is a principal one, and decoupled from the in–plane response. The difference in in–plane principal stresses is then proportional to the maximum shear stress in–plane. Fringes are generated by taking the cosine of the difference in in–plane principal stress divided by a parameter to adjust fringe density.

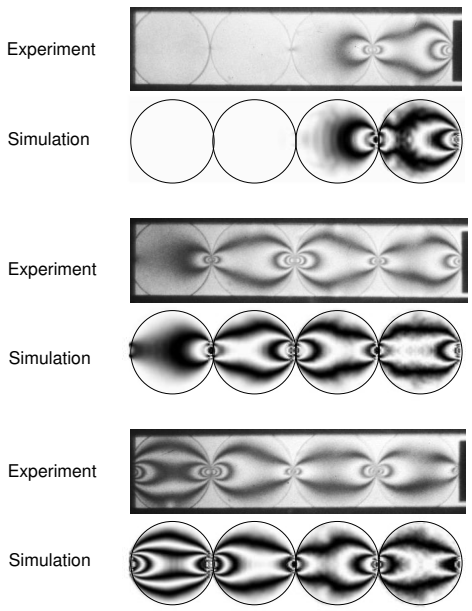

Figure 9 : Stress wave propagation through a collection of four disks with aligned centers. Matching frames are presented in pairs with the experimental data on top and simulation results below. Non–dimensional frame times are 2.6, 6.6, and 9.2 for the experimental data and 2.2, 5.5, and 7.7 for the simulation.

The numerical simulations use a linear hypoelastic constitutive model for the Plexiglas, Fung (1965). In part because the elastic constants are not known accurately for the Plexiglas used (properties can vary with manufacturer and to some degree even by material lot), and in part to facilitate a parameter study varying the elastic constants, unit geometries and wave speeds were specified in the simulations. The numerical simulations use 1 cm diameter disks and material properties resulting in a longitudinal wave speed of 1cm/μs. Specifically the material properties are shear modulus 72 GPa, bulk modulus 102 GPa and density 1900 kg/m^3. If Plexiglas was accurately modeled using hypoelasticity with the selected ratio of shear to bulk moduli, then stress magnitudes and wave speeds could be scaled by the ratio of actual to simulated moduli, and transit times could be scaled by the ratio of disk diameters, to make precise comparisons between simulations and experiments. However, the elastic constants are not known very precisely yet and, in addition, there is evidence for more complicated, rate dependent, material response, Roessig (2001). Still, purely elastic response has been found to capture gross features, as measured photoelastically, remarkably well, as seen in Fig. 9 for four collinear disks impacted on the right.

For this simple geometry, the computational resolution serves primarily to resolve the geometry, as the contact conditions are generally no slip due to the compressive loading and the geometric and material symmetry. The simulations use 80 cells across disk diameters and one material point per cell. Because of the material modeling uncertainties, the experimental results for this configuration of disks were used to determine the fringe density parameter. Matching fringe patterns were chosen by eye, subject to the constraint of equal interframe times, as in the experimental data. The same fringe density parameter is then used in all subsequent photoelastic analyses for the more complex geometries considered next.

To compare results more precisely, non–dimensional frame times are reported. The non–dimensional frame time is defined as the time after impact divided by the longitudinal wave transit time across one disk. For the simulations the longitudinal wave transit time across one disk is 1 μs. For the experiments, estimating the longitudinal wave speed as 0.27 cm/μs, Marsh (1980) results in a wave transit time of 19 μs. A selection of matching frames is shown in Fig. 9. For the experiments, the non–dimensional frame times are 2.6, 6.6, and 9.2. For the

simulations, the non–dimensional frame times are 2.2, 5.5, and 7.7. The computations accurately reproduce the experimental fringe patterns. Note that a finite exposure time results in some smoothing of the experimental images not present in the simulation data (which is instantaneous). The variation in fringe velocity through disks and across contacts is also accurately simulated. However the non–dimensional frame times are different, the fringes propagate (relatively) more quickly in the simulation.

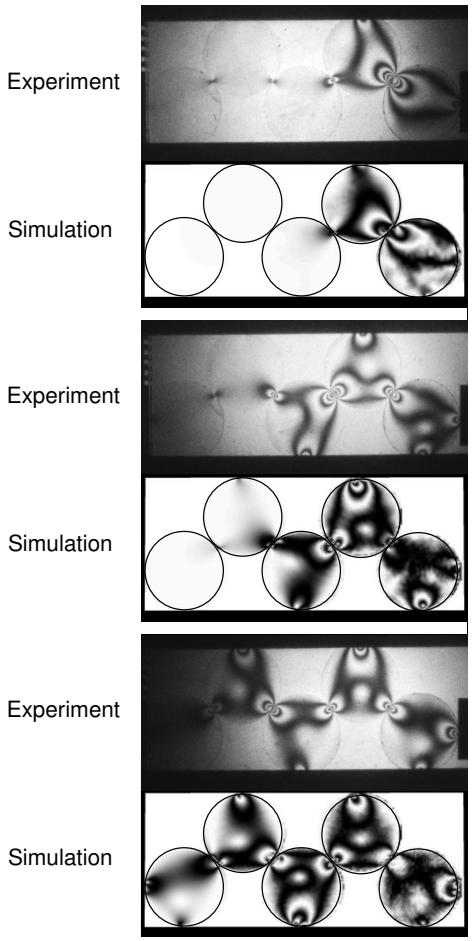

Figure 10 : Stress wave propagation through a collection of five disks with zig–zagged centers. The simulation used a friction coefficient of 0.5. Matching frames are presented in pairs with the experimental data on top and simulation results below. Non–dimensional frame times are 5.3, 10.5, and 15.8 for the experimental data and 3.0, 6.0, and 9.0 for the simulation.

A geometry which promotes slipping contact was simulated next. The disk centers were arranged such that lines connecting the centers form a 90 degree zig–zag pattern. For the simulations a coefficient of friction of 0.5 was used between the disks and contact with the walls was frictionless. Experimental and numerical results for this geometry are shown in Fig. 10 for matching fringe patterns (subject to the equal inter–frame time constraint). Matching fringe patterns were obtained at non–dimensional times of 5.3, 10.5, and 15.8 in the experiments and 3.0, 6.0, and 9.0 in the simulation. Again the fringe patterns and variations in fringe velocity are accurately simulated. In addition, other gross features are similar. Because contacts can slide, load carrying paths first develop between disk contacts and a wall. Only after sufficient normal traction builds up and the next disk contact sticks do fringes propagate into the next disk in the series. Note that the grooves in the experimental apparatus, which serve to hold the disks in plane, obscure photoelastic measurements of disk contacts with the walls. The ability of contacts to slide hinders fringe propagation across contacts and fringes propagate much more slowly in this configuration, in both the experiment and the simulation, than in the collinear disks configuration. However, the non–dimensional frame times are again in error, with fringes propagating (relatively) faster in the simulation than for the experiment, as for the collinear configuration.

To provide maximum contrast, the case was examined where the disks were glued together in the experiment to eliminate slip all altogether. No slip contact conditions were implemented between disks in the simulation by taking the coefficient of friction to be infinite. Contact with the walls remained frictionless in the simulation. Results for this case are shown in Fig. 11. Matching fringe patterns (subject to the equal inter–frame time constraint) were obtained at non–dimensional times of 1.6, 4.2, and 6.8 in the experiments and 1.4, 3.6, and 5.8 in the simulation. Again the fringe patterns and variations in fringe velocity are accurately simulated, and other gross features are similar. When contacts support shear immediately, the primary load path across a disk first develops between disk contact points. Load paths connecting disk contact points to the boundary develop later. As a result, the fringes propagate through the assembly much faster than for the same configuration with slipping contact. However, the non–dimensional frame times are again in error, with fringes propagating (relatively) faster in the simulation than in the experiment.

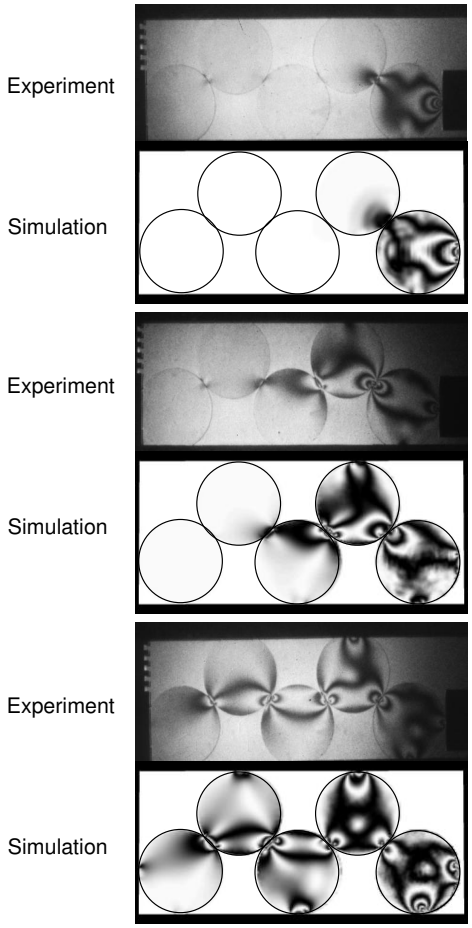

Figure 11 : Stress wave propagation through a collection of five disks with zig–zagged centers and sticking contact. Matching frames are presented in pairs with the experimental data on top and simulation results below. Non–dimensional frame times are 1.6, 4.2, and 6.8 for the experimental data and 1.4, 3.6, and 5.8 for the simulation.

The above examples indicate that contact plays an important role in stress wave propagation in collections of disks, and almost certainly plays in important role in more general granular material as well. Fringe wave speeds are strongly dependent on contact conditions, specifically the amount of slippage. The simulations are found to be in excellent qualitative agreement with the experiments. Some of the discrepancies in the details may be attributable to the boundary conditions. The disks are initially in contact with each other and the walls in the simulations, while for the experiments there are small tolerances. The biggest differences however, the systematic differences in non–dimensional frame times, are most likely due to errors in modeling material response.

A parameter study was undertaken, using the collinear disks geometry, to determine the sensitivity of fringe velocity to the Poisson's ratio, ν, keeping the longitudinal wave speed fixed. It was found that fringe velocity is strongly dependent on Poisson's ratio, but fringe patterns much less so. For the elastic constants selected, $\nu = 0.22$. A reduction in fringe velocity by more than a factor of two was obtained by increasing the Poisson's ratio from 0.22 to 0.48. This result is not unexpected, as the photoelastic technique measures gradients in shear stress, and the shear modulus (and consequently the shear wave speed) decreases with increasing Poisson's ratio. With both contact conditions and elastic constants playing important roles, a more quantitative assessment of the accuracy of the calculations awaits a better characterization of the Plexiglas' material properties. At this point it is simply noted that for a given set of material constants, the same collective fringe velocity trends are exhibited in the simulations as in the experimental data. In addition, for $\nu > 0.22$, an easily justifiable material modeling modification for polymers, the decrease in fringe velocity would tend to reduce the systematic differences in non–dimensional frame times. Better characterization of the Plexiglas used in these experiments is underway, and the results will appear in conjunction with a study of more complicated disk assemblages, Roessig (2001).

4 Conclusions

The Material Point Method provides a convenient framework for the implementation of contact between deformable bodies. The contact conditions are equivalent to a perfectly inelastic collision, providing for maximum exchange of kinetic and strain energy. For accurate application of contact under this scenario, the normal tractions must be monitored and included in the release logic. The contact calculations are computationally efficient, performed on the computational grid body by body, without requiring a search to identify neighbors. A potential numerical difficulty associated with unfortunate registration of particle information on the computational grid has been eliminated by a scaling which retains both the efficient properties of the algorithm, and conservation of momentum during contact.

The algorithm is exercised on several simple problems, for which analogous rigid body problems have analytical solutions. The algorithm is found to compare well, even

for fairly coarse discretizations with resolution of geometry the most important factor in obtaining convergence. The algorithm is exercised on a more demanding simulation involving stress propagation through collections of polymeric disks for which high fidelity experimental data is available. Excellent qualitative agreement is found for three examples with very different contact conditions. The importance of accurate simulation of material contact is demonstrated by the strong dependence of load path development and collective wave propagation speeds on the contact conditions. Other important simulation parameters were identified, including material properties and experimental tolerances. Future work will focus on obtaining better measurements of these parameters, comparing simulation to experiment quantitatively, and simulating more complex assemblages.

Acknowledgement: This work was supported by the U.S. Department of Energy through the Center for the Simulation of Accidental Fires and Explosions, under grant W-7405-ENG-48.

References

Barber, J. R.; Ciavarella, M. (2000): Contact mechanics. *International Journal of Solids and Structures*, vol. 37, pp. 29–43.

Bardenhagen, S. G. (2001): Energy conservation error in the material point method for solid mechanics. *J. Comp. Phys.* submitted.

Bardenhagen, S. G.; Brackbill, J. U. (1998): Dynamic stress bridging in granular material. *J. Appl. Phys.*, vol. 83, pp. 5732–5740.

Bardenhagen, S. G.; Brackbill, J. U.; Sulsky, D. (2000): The material-point method for granular materials. *Comput. Meths. Appld. Mechs. Engrng.*, vol. 187, pp. 529–541.

Bardenhagen, S. G.; Brackbill, J. U.; Sulsky, D. (2000): Numerical study of stress distributions in sheared granular material in two dimensions. *Phys. Rev. E*, vol. 62, pp. 3882–3890.

Bardenhagen, S. G.; Brackbill, J. U.; Sulsky, D. L. (2000): Shear deformation in granular material. In *Eleventh International Detonation Symposium*, pp. 547–555, Arlington, VA. Office of Naval Research.

Bardenhagen, S. G.; Harstad, E. N.; Maudlin, P. J.; Gray, G. T.; Foster, J. C. (1998): Viscoelastic models for explosive binder materials. *Shock Compression of Condensed Matter – 1997*, pp. 281–284.

Brackbill, J. U.; Kothe, D. B.; Ruppel, H. M. (1988): FLIP: A low-dissipation, particle-in-cell method for fluid flow. *Comput. Phys. Comm.*, vol. 48, pp. 25–38.

Brackbill, J. U.; Ruppel, H. M. (1986): FLIP: A method for adaptively zoned, particle-in-cell calculations in two dimensions. *J. Comput. Phys.*, vol. 65, pp. 314–343.

Burgess, D.; Sulsky, D.; Brackbill, J. U. (1992): Mass matrix formulation of the FLIP particle–in–cell method. *J. Comput. Phys.*, vol. 103, pp. 1–15.

Fung, Y. C. (1965): *Foundations of Solid Mechanics*. Prentice–Hall, Inc., New Jersey.

Harlow, F. H. (1963): The particle–in–cell computing method for fluid dynamics. *Meth. Comput. Phys.*, vol. 3, pp. 319.

Marsh, S. P. (1980): *LASL Shock Hugoniot Data*. University of California Press, Berkeley.

Roessig, K. M. (2001): Mesoscale mechanics of plastic bonded explosives. *Shock Compression of Condensed Matter*. to appear.

Roessig, K. M.; J.C. Foster, J. (2001): Experimental simulations of dynamic stress bridging in plastic bonded explosives. *Shock Compression of Condensed Matter*. to appear.

Rossmanith, H. P.; Shukla, A. (1982): Photoelastic investigation of dynamic load transfer in granular media. *Acta Mechanica*, vol. 42, pp. 211–225.

Shukla, A. (1991): Dynamic photoelastic studies of wave propagation in granular media. *Optics and Lasers in Engineering*, vol. 14, pp. 165–184.

Shukla, A.; Damania, C. (1987): Experimental investigation of wave velocity and dynamic contact stresses in an assembly of disks. *Experimental Mechanics*, vol. 44, pp. 268–281.

Simo, J. C.; Hughes, T. J. R. (1998): *Computational Inelasticity*. Springer-Verlag, New York.

Sulsky, D.; Chen, Z.; Schreyer, H. L. (1994): A particle method for history-dependent materials. *Comput. Methods Appl. Mech. Engrg.*, vol. 118, pp. 179–196.

Sulsky, D.; Schreyer, H. L. (1996): Axisymmetric form of the material point method with applications to upsetting and Taylor impact problems. *Comput. Meths. Appl. Mech. Engrg.*, vol. 139, pp. 409–429.

Sulsky, D.; Zhou, S.-J.; Schreyer, H. L. (1995): Application of a particle-in-cell method to solid mechanics. *Comput. Phys. Commun.*, vol. 87, pp. 236–252.

Zhong, Z.-H.; Mackerie, J. (1994): Contact–impact problems: A review with bibliography. *Appl. Mech. Rev.*, vol. 47, pp. 55–76.

Zhu, Y.; Shukla, A.; Sadd, M. H. (1996): The effect of microstructural fabric on dynamic load transfer in two dimensional assemblies of elliptical particles. *J. Mech. Phys. Solids*, vol. 44, pp. 1283–1303.